Nanoscale

Accepted Manuscript

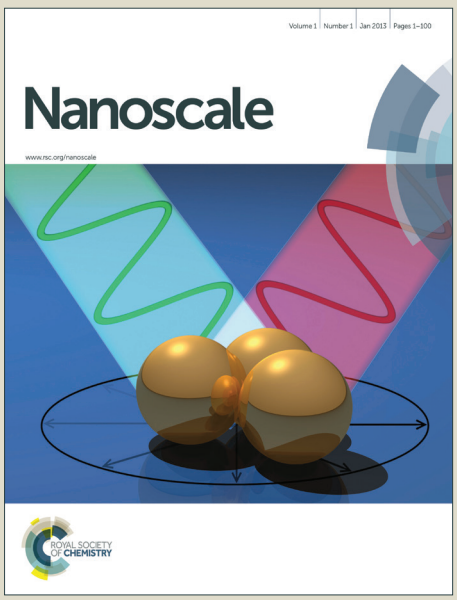

ROYAL SOCIETY OF CHEMISTRY

www.rsc.org/nanoscale

Cite this: DOI: 10.1039/c0xx00000x

www.rsc.org/xxxxxx

PAPER

Facile synthesis of three-dimensional Pt-Pd alloyed multipods with enhanced electrocatalytic activity and stability for ethylene glycol oxidation

Jing-Jing Lv, Li-Ping Mei, Xuexiang Weng, Ai-Jun Wang*, Li-Li Chen, Xiang-Feng Liu, Jiu-Ju Feng*

Received (in XXX, XXX) Xth XXXXXXXXX 20XX, Accepted Xth XXXXXXXXX 20XX
DOI: 10.1039/b000000x

A facile one-pot solvothermal method was developed for fabrication of well-defined three-dimensional highly branched Pt-Pd alloyed multipods, using ethylene glycol as a solvent and a reducing agent, along with *N*-methylimidazole as a structure-directing agent, without any seed, template, or surfactant. The as-prepared nanocrystals exhibited relatively large electrochemically active surface area, improved electrocatalytic activity and superior stability for ethylene glycol oxidation in alkaline media, compared with commercial Pt black and Pd black, making them as promising electrocatalysts in fuel cells.

Introduction

Introduction

Last several decades have witnessed great advance of noble-metal-based bimetallic alloyed nanoparticles, owing to their unique optical, catalytic, electronic, and magnetic properties,[1-3] which are distinctly different from their monometallic counterparts. In particular, Pt-based bimetallic nanomaterials have attracted considerable attention for their widespread applications in catalysis, fuel cells, and petrochemical industry.[4, 5]

Recently, a variety of Pt-based bimetallic alloys have been prepared with different features and compositions, such as Pt-Pd,[6] Pt-Au,[7] Pt-Ag,[8] and Pt-Ni alloys.[9] Among them, Pt-Pd nanocrystals show superior electrocatalytic performances in practical applications,[10-12] because the introduction of Pd into Pt can assure long-term stability and improve catalytic activity by varying the electronic structures of Pt.[2] Furthermore, the morphology of bimetallic nanocrystals strongly determines their performance.[13, 14] Thus, it is essential for shape-controlled synthesis to maximize their performance and exploit novel nanomaterials.[15, 16]

Researchers have fabricated a diversity of Pt-Pd alloyed nanostructures with unique architectural features, including spheres,[17] cages,[18] wires,[19] cubes,[20] and dendrites.[21] For example, Lim and his co-workers developed a seeded growth route for synthesis of Pt-Pd nanodendrites, using Pd nanoparticles (~9 nm) as seeds.[15] In another example, Feng's group prepared Pt-Pd nanogarlands with octylphenoxypolyethoxyethanol as a soft template via co-chemical reduction.[22] Despite these successful demonstrations, it is still a challenge to develop a facile, economic, and green synthetic route for preparing novel Pt-Pd alloyed nanomaterials with enlarged surface areas and superior performance.

Recently, a simple one-pot solvothermal/hydrothermal method has attracted remarkable interest for its high purity and large yield.[10, 23] Herein, we report a facile one-pot solvothermal method for synthesis of well-defined three-dimensional Pt-Pd alloyed multipods, using *N*-methylimidazole as a structure-directing agent and ethylene glycol (EG) as a solvent and a reducing agent. The catalytic performance of the as-prepared nanocrystals was investigated, using EG oxidation reaction in alkaline media as a general model.

Experimental

Materials

Chloroplatinic acid ($H_2PtCl_6·6H_2O$), palladium chloride ($PdCl_2$), dihydrogen hexabromoplatinate nonahydrate ($H_2PtBr_6·9H_2O$), disodium tetrabromopalladate (Na_2PdBr_4), potassium hexaiodoplatinate (K_2PtI_6), palladium iodide (PdI_2), platinum acetylacetonate ($Pt(acac)_2$), palladium acetylacetonate ($Pd(acac)_2$), *N*-methylimidazole, dimethyl formamide (DMF), EG, commercial Pt black (99.9 wt %), and Pd black (99.9 wt %) were purchased from Shanghai Aladdin Chemical Reagent Company (Shanghai, China). All the other chemicals were analytical grade and used without further purification. All the aqueous solutions were prepared with twice-distilled water.

Sample preparation

For typical synthesis of Pt-Pd multipods, 0.0177 g of $PdCl_2$ and 0.0518 g of $H_2PtCl_6·6H_2O$ were firstly dissolved into 20 mL EG solution with 5 mL *N*-methylimidazole (3.14 M). Afterward, the mixed solution was stirred for 1 h at ambient temperature. Then, the mixture was transferred into a 30 mL Teflon-lined stainless-steel autoclave and heated for 6 h at 160 °C. Next, the autoclave

was cooled to room temperature naturally. Finally, the black precipitate was collected by centrifugation, thoroughly washed with water and dried at 60 °C in a vacuum for further characterization. Meanwhile, control experiments were preformed by varying the amount of solvents, *N*-methylimidazole, different precursors or duration of reaction, while the other experimental conditions were kept unchanged.

Characterization

The morphology, composition, and elemental distribution of the samples were recorded by field emission scanning electron microscopy (SEM, JEOL JSM-6390LV, 20 kV), transmission electron microscopy (TEM), high-resolution TEM (HRTEM), X-ray energy dispersive spectra (EDS), and high angle annular bright/dark field-scanning transmission electron microscopy (HAABF-STEM/HAADF-STEM) on a JEM-2100F HR transmission electron microscope coupled with an energy-dispersive X-ray spectrometer (Oxford-1NCA). X-ray diffraction (XRD) analysis was performed on a Bruker-D8-AXS diffractometer system equipped with Cu Kα radiation (Bruker Co., Germany), and X-ray photoelectron spectroscopy (XPS) measurements was conducted by a thermofisher-ESCALAB 250Xi (ThermoFisher, E. Grinstead, UK), using AlK X-ray radiation (1486.6 eV) for excitation.

Electrochemical measurements

All electrochemical experiments were performed on a CHI 832B electrochemical workstation (CH Instruments, Chenhua Co., Shanghai, China), and performed on a conventional three-electrode cell, which includes a platinum wire as counter electrode, a saturated calomel electrode (SCE) as reference electrode, and a bare or modified glassy carbon electrode (GCE, 3 mm in diameter) as working electrode.

For typical preparation of Pt-Pd multipods modified electrodes, 1.0 mg of the sample was put into 1 mL water under ultrasonication for 30 min to obtain a homogeneous suspension (1 mg mL^{-1}). Then, 6 μL of the suspension was placed onto the clean GCE and dried in air. Next, the electrode was further coated with 5 μL Nafion (0.05 %) to seal the samples in place. Similarly, commercial Pt black- and Pd black-modified electrodes were prepared in a similar way for comparison. Thus, the specific loading of the catalysts on the electrode surface was 0.085 mg cm^{-2}.

Electrochemical CO-stripping voltammograms were obtained by oxidizing pre-adsorbed CO (CO_{ad}) in the electrolyte of 0.5 M H_2SO_4 at a scan rate of 50 mV s^{-1}. The CO was bubbled through 0.5 M H_2SO_4 for 30 min to allow complete adsorption of CO onto the deposit. The amount of the adsorbed CO was evaluated by integrating the CO_{ad} stripping peak and correcting for the capacitance of the double electric layer.

Cyclic voltammetric experiments of the catalysts were carried out in 1.0 M KOH containing 1.0 M EG at a scan rate of 50 mV s^{-1}. The chronoamperometric experiments were carried out at a fixed potential of –0.2 V. Additionally, the stability measurements were conducted by cyclic voltammetry with scanning of 2000 cycles at a scan rate of 50 mV s^{-1}. For better comparison, all the electrochemical experimental results were normalized by the geometrical surface area of the electrode (0.07065 cm^{-2}). All the experiments were preformed at room temperature, if not stated otherwise.

Results and discussion

The morphology of the typical sample was characterized by SEM and TEM measurements. As illustrated in Figure 1A, B, the product displays highly branched three-dimensional multipods and each branch presents hierarchical structures. These observations are in good accordance with the TEM image of a partial branch (Figure 1C), which contains a succession of rhombohedral segments with decreased size and the rhombohedral metamere mutually embeds one after another, as also supported by HAABF-STEM image (Figure 1E).

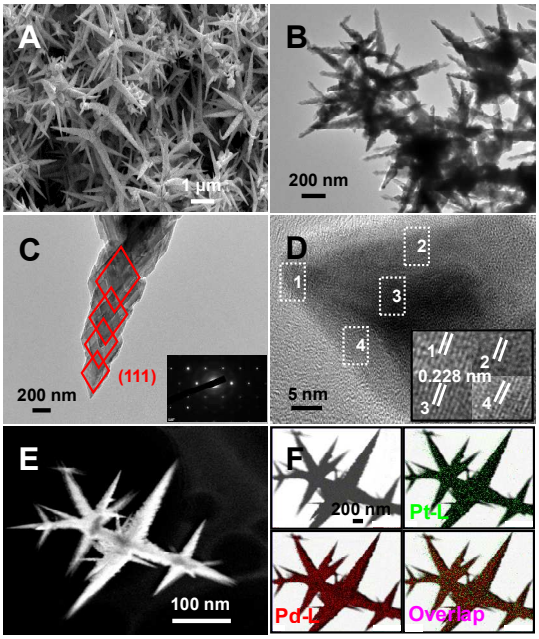

Figure 1. Representative medium-magnification SEM image (A) of Pt-Pd multipods. Typical TEM images of Pt-Pd multipods (B) and a partial arm of Pt-Pd multipods (C). HRTEM image (D) of the top part of a stem, HAADF-STEM image (E) and HAABF-STEM-EDS mapping images (F) of Pt-Pd multipods. Insets in (C) and (D) show the corresponding SAED pattern and HRTEM images of the squared areas, respectively.

The selected-area electron diffraction (SAED) pattern (Inset in Figure 1C) indicates single crystalline nature of the branch,[24] as verified by HRTEM images (Figure 1D).[25] There are well-defined lattice fringes observed at the marked regions on the top part of a stem (inset in Figure 1D), with the interplanar spacing of 0.228 nm corresponding to the (111) planes of the face-centered cubic (fcc) Pt-Pd alloy.[26] It indicates that the branches of Pt-Pd multipods have the preferential growth along the (111) directions.[27]

The HAADF-EDS mapping images (Figure 1F) are provided to examine elemental distribution of Pt-Pd multipods. Clearly, Pt and Pd are homogeneously dispersed throughout a cluster of branches, implying the formation of Pt-Pd alloyed phase.[28]

Meanwhile, EDS spectra were recorded to analyze the composition of Pt-Pd multipods, revealing the coexistence of Pt, Pd, C, and O elements (Figure 2A). The crystal structure of Pt-Pd

multipods was further determined by the XRD pattern (Figure 2B), which shows five representative diffraction peaks located at 40.16°, 46.63°, 68.18°, 82.06°, and 85.58°. These peaks are well assigned to the (111), (200), (220), (311), and (222) planes,[29] respectively, which are coincidentally located between individual Pt (JCPDS-04-0802) and Pd (JCPDS-46-1043) patterns, confirming the formation of Pt-Pd alloy.[26] Additionally, the (111) diffraction peak is sharper and stronger than the other peaks, further manifested the exposed (111) planes of Pt-Pd multipods.[30]

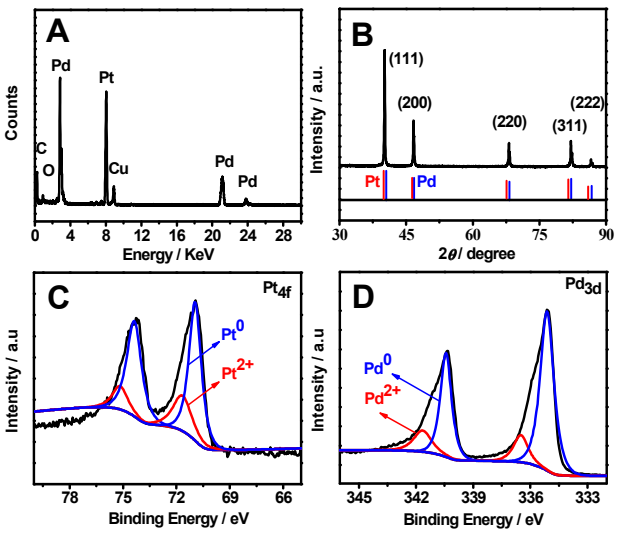

Figure 2. EDS (A), XRD (B), Pt 4f XPS (C), and Pd 3d XPS (D) spectra of Pt-Pd multipods, respectively. The standard patterns of pure Pt (JCPDS-04-0802) and Pd (JCPDS-46-1043) are attached in (B) for comparison.

XPS spectra were recorded to analyze the surface states of Pt-Pd multipods. High-resolution Pt 4f signals can be deconvoluted into two pairs of peaks (Figure 2C). Specifically, one pair is emerged at the binding energy of 74.44 and 70.96 eV, which is assigned to metallic Pt^0. The other couple locates at around 75.23 and 71.75 eV, which are ascribed to Pt^{2+} in the form of PtO and $Pt(OH)_2$.[31] Notably, the intensity of Pt^0 signals are much higher than those of Pt^{2+}, revealing that Pt^0 is the predominant species in Pt-Pd multipods.[32] Similar trend is found for high-resolution Pd 3d XPS spectrum (Figure 2D), revealing Pd^0 as the main species in Pt-Pd multipods. These results confirm efficient reduction of $PtCl_6^{2-}$ and Pd^{2+} during the solvothermal reaction process.[33]

A series of control experiments were conducted to explore the possible formation mechanism of Pt-Pd multipods. Firstly, the absence of EG produces several large spheres with many thorns on the outside surface (Figure S1A, Electronic Supplementary Information, ESI), owing to the slow reduction kinetics without EG.[34] Besides, replacing EG with DMF induces the formation of serious aggregated nanoparticles (Figure S1B, ESI), revealing the critical role of EG in dispersing Pt-Pd nanoparticles.

Most importantly, the absence of *N*-methylimidazole yields lots of aggregated nanospheres (Figure S2A, ESI), without any branched shape formed. Increasing the concentration of *N*-methylimidazole to 1.32 M produces some shorter branches (Figure S2B, ESI) as compared to the best ones under the standard conditions with 3.14 M *N*-methylimidazole (Figure 1B). This is ascribed to the relaxed growth with insufficient *N*-methylimidazole.[29] Alternatively, excess *N*-methylimidazole such as 4.37 M causes hierarchy overgrowth along the (111) planes, leading to the formation of Pt-Pd nanocrystals with much longer arms (Figure S2C, ESI). These observations strongly demonstrate the essential role of *N*-methylimidazole as a structure-directing agent for selective adsorption on the specific metallic crystal planes.[35, 36]

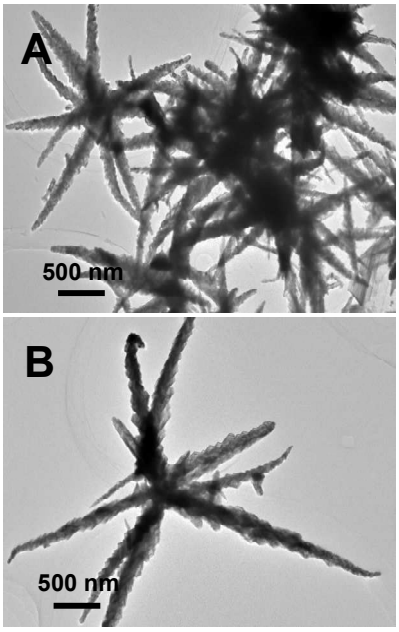

Figure 3. TEM images of the products collected by using H_2PtBr_6 and Na_2PdBr_4 (A), K_2PtI_6 and PdI_2 (B) as precursors.

To elucidate the precursor-dependent shape control, we chose different precursors, while kept all the other synthetic conditions unchanged. Interestingly, the arms of Pt-Pd multipods increase in the order of using chlorate salts (Figure 1B), bromate salts (Figure 3A), and iodate salts (Figure 3B), while the highly branched morphology almost unvaried, owing to the different adsorption effects.[37] It indicates that the halide precursors control the growth rates of the branches.

Alternatively, only using $PdCl_2$ as the precursor causes the formation of agminated nanoparticles with short branches (Figure S3, ESI), while nearly no product is obtained for H_2PtCl_6 as the precursor. This is ascribed to the relatively lower standard reduction potential of $PtCl_6^{2-}$/Pt (0.73 V *vs*. SHE) than that of Pd^{2+}/Pd (0.92 V *vs*. SHE). These observations verify the key role of Pd in the nucleation process,[35] while Pt promotes the growth rate through binding with *N*-methylimidazole.[38] On the other hand, using $Pt(acac)_2$ and $Pd(acac)_2$ as the precursors, rather than H_2PtCl_6 and $PdCl_2$, only some irregular structures are formed, instead of Pt-Pd multipods (Figure S4, ESI). It is attributed to the variation of reduction kinetics by using different precursors.[39]

Time-dependent TEM experiments were performed to monitor the morphology evolution of Pt-Pd multipods during the hydrothermal process. As illustrated in Figure 4, numerous scattered nanoparticles are emerged after the reaction of 1 h

(Figure 4A), which are gradually aggregated together to form polyhedron nuclei within the reaction time of 2 h (Figure 4B) via heterogeneous nucleation and self-assembly.[40] The newly generated Pt and Pd atoms grow along the (111) planes from the initial nuclei, with the orientation role of Pt precursor-*N*-methylimidazole complex that can decrease the surface energy of the present system.[24, 38, 41] Immature multipods of Pt-Pd nanocrystals are generated by increasing the reaction time to 4 h (Figure 4C), and their arms continually increase with the reaction time even up to 6 h (Figure 1B), owing to the subsequent attachment of newly formed Pt and Pd atoms onto the (111) planes.[42] Nevertheless, the shape of Pt-Pd nanocrystals almost remains unchanged by further prolonging the reaction time to 8 h (Figure 4D).

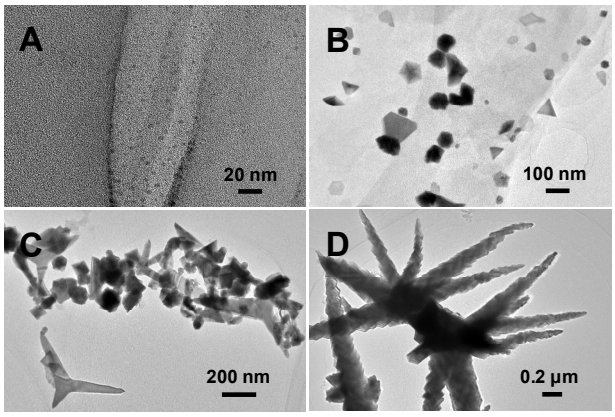

Figure 4. TEM images of the products collected at different reaction time: (A) 1 h, (B) 2 h, (C) 4 h, and (D) 8 h.

Figure 5 describes the formation mechanism of Pt-Pd multipods. The Pt and Pd precursors are gradually reduced to Pt and Pd atoms by EG. Meanwhile, the Pt precursor-*N*-methylimidazole complex is formed to direct the subsequent crystal growth, owing to its stronger binding affinity to N-containing molecules in comparison with that of the Pd precursor.[38, 43] Once the concentrations of the newly formed Pt and Pd atoms achieve the level of supersaturation, they begin to develop into polyhedral nuclei for decreasing the whole system surface free energy.[40] Afterward, the polyhedral nuclei undergo the epitaxial growth, along with elongating the corner of polyhedron.[27, 44] Last but not the least, Pt-Pd multipods with arms containing a succession of rhombohedral scleromeres are formed through multi-generation overgrowth at the tips and edges of the crystals.[45]

Figure S5 (ESI) shows the cyclic voltammograms (CVs) of Pt-Pd multipods (Figure S5A, ESI), Pt black (Figure S5B, ESI) and Pd black (Figure S5C, ESI) catalyst-modified electrodes in 0.5 M H_2SO_4 after the CO-stripping treatment. Based on the oxidation peak from the first (1st) cycle, the electrochemically active surface area (ECSA) of Pt-Pd multipods is calculated to be 20.6 $m^2\ g^{-1}$ (Figure S5D, ESI), which is much higher than those of Pt black (7.3 $m^2\ g^{-1}$) and Pd black (10.9 $m^2\ g^{-1}$).[35, 46, 47] It suggests more active sites available for Pt-Pd multipods in comparison with commercial Pt black and Pd black, which would endow them with improved electrocatalytic performance.[48]

Besides, the typical CVs of Pt-Pd multipods (curve a), Pt black (curve b) and Pd black (curve c) catalyst-modified electrodes were obtained in 0.5 M H_2SO_4 at a scan rate of 50 mV s^{-1} (Figure S6, ESI). All the samples display a strong peak, corresponding to proton reduction/hydrogen oxidation below 0.1 V.[49] The peak current densities in the hydrogen adsorption/desorption and oxide formation/reduction regions decrease in the order of Pt-Pd multipods, Pt black, and Pd black, strongly showing the larger ECSA of Pt-Pd multipods. It reveals that Pt-Pd multipods would have potential higher catalytic activity as a catalyst.[13]

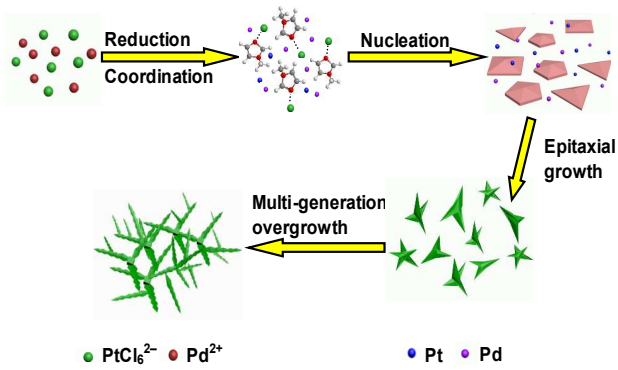

Figure 5. Schematic illustration for the formation mechanism of Pt-Pd multipods.

Herein, Pt-Pd multipods were applied as a catalyst for EG oxidation in alkaline media, using commercial Pt black and Pd black as references. As displayed in Figure 6A, each of them shows two obvious anodic peaks in their corresponding CVs, which are the typical features for EG oxidation during the forward and backward scans.[50] Clearly, Pt-Pd multipods exhibit the highest electrocatalytic current density among the catalysts, evidencing the enhanced catalytic activity of Pt-Pd multipods.[51]

Meanwhile, the onset potential of Pt-Pd multipods is ca. –0.71 V, which is more positive than Pt black (–0.75 V), but more negative than Pd black (–0.56 V). These phenomena strongly manifest the formation of Pt-Pd alloy, as supported by HAABF-STEM-EDS mapping images and XRD analysis. Furthermore, the ratio of the peak current densities associated with the anodic peaks in forward (j_F) and reverse (j_R) is 3.64 for Pt-Pd multipods, which is larger than Pd black (2.58), while smaller than Pt black (4.92) under the same conditions, owing to the modified electronic structure of Pt by the introduction of Pd. Additionally, the value of j_F/j_R of Pt-Pd multipods is much higher than those of SF-MWCNT-Pd (1.82),[52] Pd/C (2.74),[53] S-MWNTs/Pd (1.94),[54] and hAg@Pt–RGO (1.72) in the literature,[55] illustrating better CO resistance activity of Pt-Pd multipods.[56]

To compare the catalytic activity for different catalysts, the current densities of anodic peak for Pt-Pd multipods, Pt black, and Pd black were normalized with respect to the loading amount and ECSA of a catalyst, respectively. As listed in Figure 6B, the mass activity (current per unit gram of catalyst) of Pt-Pd multipods is higher than those of Pt black and Pd black. The specific activity (current per unit per surface area of catalyst) is slightly lower than that of Pt black, while higher than that of Pd

black. These results further demonstrate that Pt-Pd multipods have superior catalytic activity toward EG electrooxidation.

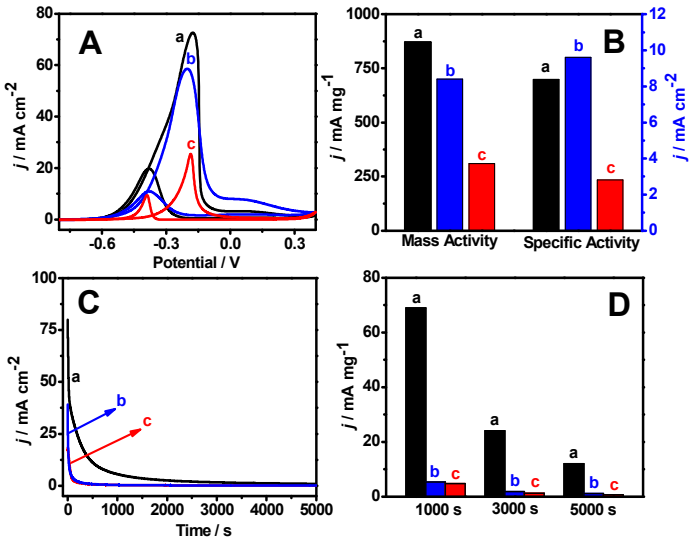

Figure 6. CVs (A) of the Pt-Pd multipods (curve a), Pt black (curve b), and Pd black (curve c) catalyst-modified electrodes in 1.0 M KOH + 1 M EG at a scan rate of 50 mV s^{-1}. The corresponding mass and specific activities (B) at the associated anodic peak potentials. The chronoamperometric curves (C) of the Pt-Pd multipods (curve a), Pt black (curve b), and Pd black (curve c) catalyst-modified electrodes at a fixed potential of –0.2 V. The corresponding mass activities (D) at different measured time.

The catalytic stability of Pt-Pd multipods, Pt black, and Pd black were examined by chronoamperometric experiments tested at –0.2 V for 5000 s (Figure 6C). Clearly, Pt-Pd multipods own higher catalytic current intensities and a slower dropping rate, compared with those of Pt black and Pd black under the identical conditions. Meanwhile, the corresponding mass activity of Pt-Pd multipods, Pt black, and Pd black were provided at the measured time of 1000, 3000, and 5000 s (Figure 6D). Obviously, Pt-Pd multipods decay much slower and remain comparatively higher mass activity after the chronoamperometric measurements, in comparison with those of Pt black and Pd black, revealing improved durability of Pt-Pd multipods.[57, 58]

To get deep insight into the catalytic durability of Pt-Pd multipods, the CVs were recorded in 1.0 M KOH containing 1 M EG for 2000 cycles, using Pt black and Pd black as referenced materials. It is found that the anodic peak current densities of Pt-Pd multipods remain 54.79 % and 44.04 % of the initial values after 1000 and 2000 cycles (Figure 7A), respectively. Nevertheless, the anodic peak current densities of Pt black (Figure 7B) and Pd black (Figure 7C) retain 0.052 % and 57.59 % after 1000 cycles, and 0.0096 % and 29.34 % after 2000 cycles, respectively. Additionally, the anodic peak current densities of Pt-Pd multipods slightly decrease over 2000 cycles (Figure 7D) as compared to Pt black and Pd black. These phenomena demonstrate the long-term durability of Pt-Pd multipods.[59]

All the above electrochemical experimental data confirm that Pt-Pd multipods can serve as an ideal catalyst for direct EG fuel cells, which would contribute to the following reasons. Firstly, Pt-Pd multipods possess much more accessible surface active sites because of their three-dimensional highly branched structures with various rhombohedral scleromeres.[60] Besides, the unique interconnected three-dimensional nanostructures make Pt-Pd multipods less vulnerable to dissolution and aggregation than those of the zero-dimensional Pt black and Pd black (Figure S7, ESI), and thereby improve its electrocatalytic stability.[9, 48] Moreover, the synergistic effects between Pt and Pd effectively enhance the electrocatalytic activity of Pt-Pd multipods.[11, 38]

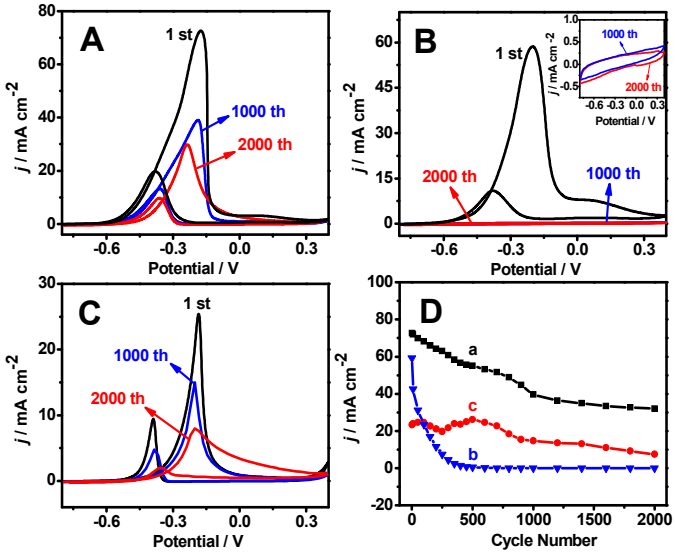

Figure 7. The 1st, 1000th, and 2000th CVs of the Pt-Pd multipods (A), Pt black (B) and Pd black (C) catalyst-modified electrodes in 1.0 M KOH + 1 M EG, respectively. The forward peak current density (*j*) as a function of potential scanning cycles (D) of the Pt-Pd multipods (curve a), Pt black (curve b), and Pd black (curve c) catalyst-modified electrodes. Inset in (B) show the corresponding high-resolution 1000th and 2000th CVs for Pt black catalyst-modified electrode.

Conclusions

In summary, we have developed a facile, efficient, and clean strategy for synthesis of three-dimensional Pt-Pd alloyed multipods under solvolthermal conditions by applying EG as a reducing agent and solvent, and *N*-methylimidazole as a structure-directing agent. The possible formation mechanism of Pt-Pd multipods was discussed, in which involves the nucleation, epitaxial growth, and multi-generation overgrowth processes. More importantly, the as-prepared Pt-Pd multipods displayed the enlarged ECSA, enhanced electrocatalytic activity, and long-term stability toward EG oxidation reaction, proving it as a highly efficient catalyst for direct alcohol fuel cells.

Acknowledgements

This work was financially supported by National Natural Science Foundation of China (21475118, 21175118 and 21275130) and colleges in Zhejiang province to the young academic leaders of academic climbing project (pd2013055).

Notes and references

College of Geography and Environmental Science, College of Chemistry and Life Science, Zhejiang Normal University, Jinhua 321004, China

**Corresponding Author: Tel./Fax:+86 579 82282269. Email: ajwang@zjnu.cn (AJW); jjfeng@zjnu.cn (JJF).*

1 L. Dai, Y. Zhao, Q. Chi, T. Huang and H. Liu, *CrystEngComm*, 2014, **16**, 5206-5211.

2 H. Zhang, M. Jin and Y. Xia, *Chem. Soc. Rev.*, 2012, **41**, 8035-8049.

3 X. Liu, D. Wang and Y. Li, *Nano Today*, 2012, **7**, 448-466.

4 Y. Liu, D. Li and S. Sun, *J. Mater. Chem.*, 2011, **21**, 12579-12587.

5 N. S. Porter, H. Wu, Z. Quan and J. Fang, *Acc. Chem. Res.*, 2013, **46**, 1867-1877.

6 Y.-W. Lee, A. R. Ko, D.-Y. Kim, S.-B. Han and K.-W. Park, *RSC Adv.*, 2012, **2**, 1119-1125.

7 Y. Yamauchi, A. Tonegawa, M. Komatsu, H. Wang, L. Wang, Y. Nemoto, N. Suzuki and K. Kuroda, *J. Am. Chem. Soc.*, 2012, **134**, 5100-5109.

8 Y.-Y. Feng, L.-X. Bi, Z.-H. Liu, D.-S. Kong and Z.-Y. Yu, *J. Catal.*, 2012, **290**, 18-25.

9 X. Huang, E. Zhu, Y. Chen, Y. Li, C.-Y. Chiu, Y. Xu, Z. Lin, X. Duan and Y. Huang, *Adv. Mater.*, 2013, **25**, 2974-2979.

10 A.-X. Yin, X.-Q. Min, W. Zhu, H.-S. Wu, Y.-W. Zhang and C.-H. Yan, *Chem. Commun.*, 2012, **48**, 543-545.

11 Z.-C. Zhang, J.-F. Hui, Z.-G. Guo, Q.-Y. Yu, B. Xu, X. Zhang, Z.-C. Liu, C.-M. Xu, J.-S. Gao and X. Wang, *Nanoscale*, 2012, **4**, 2633-2639.

12 Z. Chen, M. Waje, W. Li and Y. Yan, *Angew. Chem. Int. Ed.*, 2007, **46**, 4060-4063.

13 L. Wang and Y. Yamauchi, *Chem. Mater.*, 2009, **21**, 3562-3569.

14 B. Lim and Y. Xia, *Angew. Chem. Int. Ed.*, 2011, **50**, 76-85.

15 B. Lim, M. Jiang, P. H. C. Camargo, E. C. Cho, J. Tao, X. Lu, Y. Zhu and Y. Xia, *Science*, 2009, **324**, 1302-1305.

16 X. Chen, Z. Cai, X. Chen and M. Oyama, *J. Mater. Chem. A*, 2014, **2**, 315-320.

17 B. Liu, H. Y. Li, L. Die, X. H. Zhang, Z. Fan and J. H. Chen, *J. Power Sources*, 2009, **186**, 62-66.

18 H. Zhang, M. Jin, H. Liu, J. Wang, M. J. Kim, D. Yang, Z. Xie, J. Liu and Y. Xia, *ACS Nano*, 2011, **5**, 8212-8222.

19 S. Guo, S. Dong and E. Wang, *Chem. Commun.*, 2010, **46**, 1869-1871.

20 X. Chen, Z. Cai, X. Chen and M. Oyama, *Carbon*, 2014, **66**, 387-394.

21 S. Guo, S. Dong and E. Wang, *ACS Nano*, 2009, **4**, 547-555.

22 S.-S. Li, J.-N. Zheng, X. Ma, Y.-Y. Hu, A.-J. Wang, J. Chen and J.-J. Feng, *Nanoscale*, 2014, **6**, 5708-5713.

23 T. Kim, J. Lian, J. Ma, X. Duan and W. Zheng, *Cryst. Growth Des.*, 2010, **10**, 2928-2933.

24 R. Zhao, G. Fu, T. Zhou, Y. Chen, X. Zhu, Y. Tang and T. Lu, *Nanoscale*, 2014, **6**, 2776-2781.

25 G. Fu, X. Jiang, M. Gong, Y. Chen, Y. Tang, J. Lin and T. Lu, *Nanoscale*, 2014, **6**, 8226-8234.

26 X. Yang, Q. Yang, J. Xu and C.-S. Lee, *J. Mater. Chem.*, 2012, **22**, 8057-8062.

27 S. Maksimuk, X. Teng and H. Yang, *J. Phys. Chem. C*, 2007, **111**, 14312-14319.

28 Y. Lu, Y. Jiang and W. Chen, *Nano Energy*, 2013, **2**, 836-844.

29 H. Zhu, G. Li, X. Lv, Y. Zhao, T. Huang, H. Liu and J. Li, *RSC Adv.*, 2014, **4**, 6535-6539.

30 B. Y. Xia, H. B. Wu, Y. Yan, X. W. Lou and X. Wang, *J. Am. Chem. Soc.*, 2013, **135**, 9480-9485.

31 J. Yang, W. Zhou, C. H. Cheng, J. Y. Lee and Z. Liu, *ACS Appl. Mat. Interfaces*, 2010, **2**, 119-126.

32 G. Fu, K. Wu, J. Lin, Y. Tang, Y. Chen, Y. Zhou and T. Lu, *J. Phys. Chem. C*, 2013, **117**, 9826-9834.

33 Y. Lu, Y. Jiang and W. Chen, *Nanoscale*, 2014, **6**, 3309-3315.

34 L. S. Sarma, C.-H. Chen, S. M. S. Kumar, G.-R. Wang, S.-C. Yen, D.-G. Liu, H.-S. Sheu, K.-L. Yu, M.-T. Tang, J.-F. Lee, C. Bock, K.-H. Chen and B.-J. Hwang, *Langmuir*, 2007, **23**, 5802-5809.

35 J.-J. Lv, J.-N. Zheng, S.-S. Li, L.-L. Chen, A.-J. Wang and J.-J. Feng, *J. Mater. Chem. A*, 2014, **2**, 4384-4390.

36 J.-J. Lv, J.-N. Zheng, Y.-Y. Wang, A.-J. Wang, L.-L. Chen and J.-J. Feng, *J. Power Sources*, 2014, **265**, 231-238.

37 M. Chen, B. Wu, J. Yang and N. Zheng, *Adv. Mater.*, 2012, **24**, 862-879.

38 S. W. Kang, Y. W. Lee, Y. Park, B.-S. Choi, J. W. Hong, K.-H. Park and S. W. Han, *ACS Nano*, 2013, **7**, 7945-7955.

39 X. Huang, H. Zhang, C. Guo, Z. Zhou and N. Zheng, *Angew. Chem. Int. Ed.*, 2009, **48**, 4808-4812.

40 Y. Wang, S.-I. Choi, X. Zhao, S. Xie, H.-C. Peng, M. Chi, C. Z. Huang and Y. Xia, *Adv. Funct. Mater.*, 2014, **24**, 131-139.

41 B. Lim, M. Jiang, T. Yu, P. C. Camargo and Y. Xia, *Nano Res.*, 2010, **3**, 69-80.

42 S. Maksimuk, X. Teng and H. Yang, *Phys. Chem. Chem. Phys.*, 2006, **8**, 4660-4663.

43 C. J. DeSantis, A. A. Peverly, D. G. Peters and S. E. Skrabalak, *Nano Lett.*, 2011, **11**, 2164-2168.

44 L. Zhang, S.-I. Choi, J. Tao, H.-C. Peng, S. Xie, Y. Zhu, Z. Xie and Y. Xia, *Adv. Funct. Mater.*, 2014, **24**, 7520-7529.

45 W. Wang, Y. Han, M. Gao and Y. Wang, *CrystEngComm*, 2013, **15**, 2648-2656.

46 M. J. Watt-Smith, J. M. Friedrich, S. P. Rigby, T. R. Ralph and F. C. Walsh, *J. Phys. D: Appl. Phys.*, 2008, **41**, 174004-174012.

47 C. Hu, Z. Bai, L. Yang, J. Lv, K. Wang, Y. Guo, Y. Cao and J. zhou, *Electrochim. Acta*, 2010, **55**, 6036-6041.

48 X. Huang, Y. Li, Y. Chen, E. Zhou, Y. Xu, H. Zhou, X. Duan and Y. Huang, *Angew. Chem.*, 2013, **125**, 2580-2584.

49 C. Zhu, S. Guo and S. Dong, *Chem. Eur. J.*, 2013, **19**, 1104-1111.

50 V. Selvaraj, M. Vinoba and M. Alagar, *J. Colloid Interface Sci.*, 2008, **322**, 537-544.

51 F. Li, Y. Guo, R. Li, F. Wu, Y. Liu, X. Sun, C. Li, W. Wang and J. Gao, *J. Mater. Chem. A*, 2013, **1**, 6579-6587.

52 T. Ramulifho, K. I. Ozoemena, R. M. Modibedi, C. J. Jafta and M. K. Mathe, *J. Electroanal. Chem.*, 2013, **692**, 26-30.

53 O. O. Fashedemi and K. I. Ozoemena, *Electrochim. Acta*, 2014, **128**, 279-286.

54 Z.-P. Sun, X.-G. Zhang, Y.-Y. Liang and H.-L. Li, *J. Power Sources*, 2009, **191**, 366-370.

55 J.-N. Zheng, J.-J. Lv, S.-S. Li, M.-W. Xue, A.-J. Wang and J.-J. Feng, *J. Mater. Chem. A*, 2014, **2**, 3445-3451.

56 Y.-N. Wu, S.-J. Liao, Z.-X. Liang, L.-J. Yang and R.-F. Wang, *J.*

Power Sources, 2009, **194**, 805-810.
57 B. Y. Xia, H. B. Wu, X. Wang and X. W. Lou, *J. Am. Chem. Soc.*, 2012, **134**, 13934-13937.
58 F. Zhan, T. Bian, W. Zhao, H. Zhang, M. Jin and D. Yang, *CrystEngComm*, 2014, **16**, 2411-2416.
59 C. Hu, H. Cheng, Y. Zhao, Y. Hu, Y. Liu, L. Dai and L. Qu, *Adv. Mater.*, 2012, **24**, 5493-5498.
60 K. Kakaei, *Carbon*, 2013, **51**, 195-201.

Cite this: DOI: 10.1039/c0xx00000x

www.rsc.org/xxxxxx

PAPER

Facile synthesis of three-dimensional Pt-Pd alloyed multipods with enhanced electrocatalytic activity and stability for ethylene glycol oxidation

Jing-Jing Lv, Li-Ping Mei, Xuexiang Weng, Ai-Jun Wang*, Li-Li Chen, Xiang-Feng Liu, Jiu-Ju Feng*

Received (in XXX, XXX) Xth XXXXXXXXX 20XX, Accepted Xth XXXXXXXXX 20XX
DOI: 10.1039/b000000x

A facile one-pot solvothermal method was developed for fabrication of well-defined three-dimensional highly branched Pt-Pd alloyed multipods, using ethylene glycol as a solvent and a reducing agent, along with *N*-methylimidazole as a structure-directing agent, without any seed, template, or surfactant. The as-prepared nanocrystals exhibited relatively large electrochemically active surface area, improved electrocatalytic activity and superior stability for ethylene glycol oxidation in alkaline media, compared with commercial Pt black and Pd black, making them as promising electrocatalysts in fuel cells.

Introduction

Introduction

Last several decades have witnessed great advance of noble-metal-based bimetallic alloyed nanoparticles, owing to their unique optical, catalytic, electronic, and magnetic properties,[1-3] which are distinctly different from their monometallic counterparts. In particular, Pt-based bimetallic nanomaterials have attracted considerable attention for their widespread applications in catalysis, fuel cells, and petrochemical industry.[4, 5]

Recently, a variety of Pt-based bimetallic alloys have been prepared with different features and compositions, such as Pt-Pd,[6] Pt-Au,[7] Pt-Ag,[8] and Pt-Ni alloys.[9] Among them, Pt-Pd nanocrystals show superior electrocatalytic performances in practical applications,[10-12] because the introduction of Pd into Pt can assure long-term stability and improve catalytic activity by varying the electronic structures of Pt.[2] Furthermore, the morphology of bimetallic nanocrystals strongly determines their performance.[13, 14] Thus, it is essential for shape-controlled synthesis to maximize their performance and exploit novel nanomaterials.[15, 16]

Researchers have fabricated a diversity of Pt-Pd alloyed nanostructures with unique architectural features, including spheres,[17] cages,[18] wires,[19] cubes,[20] and dendrites.[21] For example, Lim and his co-workers developed a seeded growth route for synthesis of Pt-Pd nanodendrites, using Pd nanoparticles (~9 nm) as seeds.[15] In another example, Feng's group prepared Pt-Pd nanogarlands with octylphenoxypolyethoxyethanol as a soft template via co-chemical reduction.[22] Despite these successful demonstrations, it is still a challenge to develop a facile, economic, and green synthetic route for preparing novel Pt-Pd alloyed nanomaterials with enlarged surface areas and superior performance.

Recently, a simple one-pot solvothermal/hydrothermal method has attracted remarkable interest for its high purity and large yield.[10, 23] Herein, we report a facile one-pot solvothermal method for synthesis of well-defined three-dimensional Pt-Pd alloyed multipods, using *N*-methylimidazole as a structure-directing agent and ethylene glycol (EG) as a solvent and a reducing agent. The catalytic performance of the as-prepared nanocrystals was investigated, using EG oxidation reaction in alkaline media as a general model.

Experimental

Materials

Chloroplatinic acid ($H_2PtCl_6·6H_2O$), palladium chloride ($PdCl_2$), dihydrogen hexabromoplatinate nonahydrate ($H_2PtBr_6·9H_2O$), disodium tetrabromopalladate (Na_2PdBr_4), potassium hexaiodoplatinate (K_2PtI_6), palladium iodide (PdI_2), platinum acetylacetonate ($Pt(acac)_2$), palladium acetylacetonate ($Pd(acac)_2$), *N*-methylimidazole, dimethyl formamide (DMF), EG, commercial Pt black (99.9 wt %), and Pd black (99.9 wt %) were purchased from Shanghai Aladdin Chemical Reagent Company (Shanghai, China). All the other chemicals were analytical grade and used without further purification. All the aqueous solutions were prepared with twice-distilled water.

Sample preparation

For typical synthesis of Pt-Pd multipods, 0.0177 g of $PdCl_2$ and 0.0518 g of $H_2PtCl_6·6H_2O$ were firstly dissolved into 20 mL EG solution with 5 mL *N*-methylimidazole (3.14 M). Afterward, the mixed solution was stirred for 1 h at ambient temperature. Then, the mixture was transferred into a 30 mL Teflon-lined stainless-steel autoclave and heated for 6 h at 160 °C. Next, the autoclave

was cooled to room temperature naturally. Finally, the black precipitate was collected by centrifugation, thoroughly washed with water and dried at 60 °C in a vacuum for further characterization. Meanwhile, control experiments were preformed by varying the amount of solvents, *N*-methylimidazole, different precursors or duration of reaction, while the other experimental conditions were kept unchanged.

Characterization

The morphology, composition, and elemental distribution of the samples were recorded by field emission scanning electron microscopy (SEM, JEOL JSM-6390LV, 20 kV), transmission electron microscopy (TEM), high-resolution TEM (HRTEM), X-ray energy dispersive spectra (EDS), and high angle annular bright/dark field-scanning transmission electron microscopy (HAABF-STEM/HAADF-STEM) on a JEM-2100F HR transmission electron microscope coupled with an energy-dispersive X-ray spectrometer (Oxford-1NCA). X-ray diffraction (XRD) analysis was performed on a Bruker-D8-AXS diffractometer system equipped with Cu Kα radiation (Bruker Co., Germany), and X-ray photoelectron spectroscopy (XPS) measurements was conducted by a thermofisher-ESCALAB 250Xi (ThermoFisher, E. Grinstead, UK), using AlK X-ray radiation (1486.6 eV) for excitation.

Electrochemical measurements

All electrochemical experiments were performed on a CHI 832B electrochemical workstation (CH Instruments, Chenhua Co., Shanghai, China), and performed on a conventional three-electrode cell, which includes a platinum wire as counter electrode, a saturated calomel electrode (SCE) as reference electrode, and a bare or modified glassy carbon electrode (GCE, 3 mm in diameter) as working electrode.

For typical preparation of Pt-Pd multipods modified electrodes, 1.0 mg of the sample was put into 1 mL water under ultrasonication for 30 min to obtain a homogeneous suspension (1 mg mL^{-1}). Then, 6 μL of the suspension was placed onto the clean GCE and dried in air. Next, the electrode was further coated with 5 μL Nafion (0.05 %) to seal the samples in place. Similarly, commercial Pt black- and Pd black-modified electrodes were prepared in a similar way for comparison. Thus, the specific loading of the catalysts on the electrode surface was 0.085 mg cm^{-2}.

Electrochemical CO-stripping voltammograms were obtained by oxidizing pre-adsorbed CO (CO_{ad}) in the electrolyte of 0.5 M H_2SO_4 at a scan rate of 50 mV s^{-1}. The CO was bubbled through 0.5 M H_2SO_4 for 30 min to allow complete adsorption of CO onto the deposit. The amount of the adsorbed CO was evaluated by integrating the CO_{ad} stripping peak and correcting for the capacitance of the double electric layer.

Cyclic voltammetric experiments of the catalysts were carried out in 1.0 M KOH containing 1.0 M EG at a scan rate of 50 mV s^{-1}. The chronoamperometric experiments were carried out at a fixed potential of –0.2 V. Additionally, the stability measurements were conducted by cyclic voltammetry with scanning of 2000 cycles at a scan rate of 50 mV s^{-1}. For better comparison, all the electrochemical experimental results were normalized by the geometrical surface area of the electrode (0.07065 cm^{-2}). All the experiments were preformed at room temperature, if not stated otherwise.

Results and discussion

The morphology of the typical sample was characterized by SEM and TEM measurements. As illustrated in Figure 1A, B, the product displays highly branched three-dimensional multipods and each branch presents hierarchical structures. These observations are in good accordance with the TEM image of a partial branch (Figure 1C), which contains a succession of rhombohedral segments with decreased size and the rhombohedral metamere mutually embeds one after another, as also supported by HAABF-STEM image (Figure 1E).

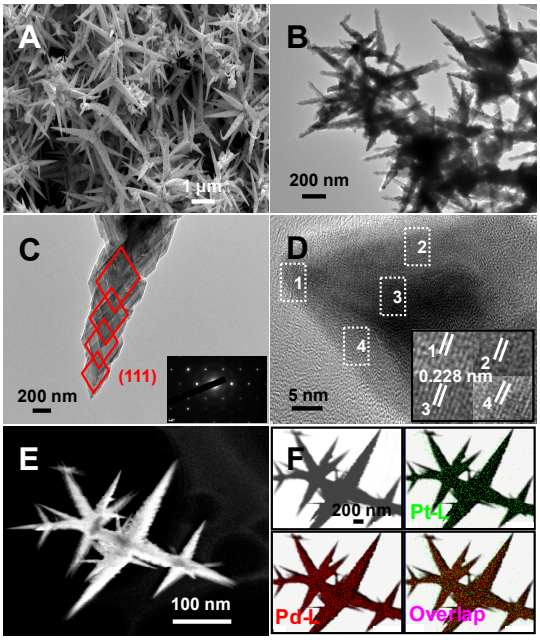

Figure 1. Representative medium-magnification SEM image (A) of Pt-Pd multipods. Typical TEM images of Pt-Pd multipods (B) and a partial arm of Pt-Pd multipods (C). HRTEM image (D) of the top part of a stem, HAADF-STEM image (E) and HAABF-STEM-EDS mapping images (F) of Pt-Pd multipods. Insets in (C) and (D) show the corresponding SAED pattern and HRTEM images of the squared areas, respectively.

The selected-area electron diffraction (SAED) pattern (Inset in Figure 1C) indicates single crystalline nature of the branch,[24] as verified by HRTEM images (Figure 1D).[25] There are well-defined lattice fringes observed at the marked regions on the top part of a stem (inset in Figure 1D), with the interplanar spacing of 0.228 nm corresponding to the (111) planes of the face-centered cubic (fcc) Pt-Pd alloy.[26] It indicates that the branches of Pt-Pd multipods have the preferential growth along the (111) directions.[27]

The HAADF-EDS mapping images (Figure 1F) are provided to examine elemental distribution of Pt-Pd multipods. Clearly, Pt and Pd are homogeneously dispersed throughout a cluster of branches, implying the formation of Pt-Pd alloyed phase.[28]

Meanwhile, EDS spectra were recorded to analyze the composition of Pt-Pd multipods, revealing the coexistence of Pt, Pd, C, and O elements (Figure 2A). The crystal structure of Pt-Pd

multipods was further determined by the XRD pattern (Figure 2B), which shows five representative diffraction peaks located at 40.16°, 46.63°, 68.18°, 82.06°, and 85.58°. These peaks are well assigned to the (111), (200), (220), (311), and (222) planes,[29] respectively, which are coincidentally located between individual Pt (JCPDS-04-0802) and Pd (JCPDS-46-1043) patterns, confirming the formation of Pt-Pd alloy.[26] Additionally, the (111) diffraction peak is sharper and stronger than the other peaks, further manifested the exposed (111) planes of Pt-Pd multipods.[30]

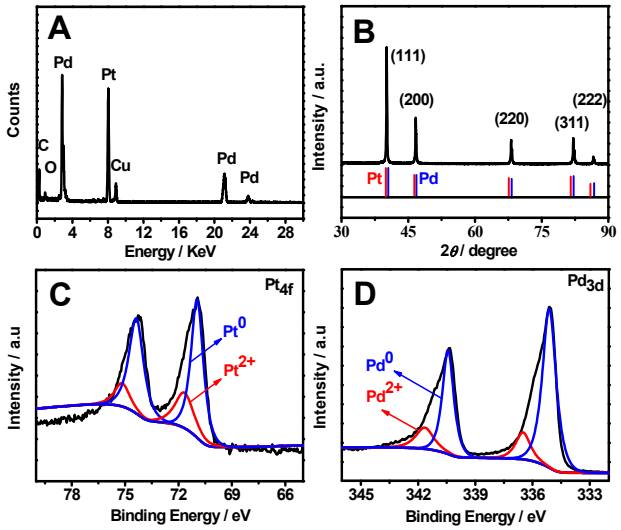

Figure 2. EDS (A), XRD (B), Pt 4f XPS (C), and Pd 3d XPS (D) spectra of Pt-Pd multipods, respectively. The standard patterns of pure Pt (JCPDS-04-0802) and Pd (JCPDS-46-1043) are attached in (B) for comparison.

XPS spectra were recorded to analyze the surface states of Pt-Pd multipods. High-resolution Pt 4f signals can be deconvoluted into two pairs of peaks (Figure 2C). Specifically, one pair is emerged at the binding energy of 74.44 and 70.96 eV, which is assigned to metallic Pt^0. The other couple locates at around 75.23 and 71.75 eV, which are ascribed to Pt^{2+} in the form of PtO and $Pt(OH)_2$.[31] Notably, the intensity of Pt^0 signals are much higher than those of Pt^{2+}, revealing that Pt^0 is the predominant species in Pt-Pd multipods.[32] Similar trend is found for high-resolution Pd 3d XPS spectrum (Figure 2D), revealing Pd^0 as the main species in Pt-Pd multipods. These results confirm efficient reduction of $PtCl_6^{2-}$ and Pd^{2+} during the solvothermal reaction process.[33]

A series of control experiments were conducted to explore the possible formation mechanism of Pt-Pd multipods. Firstly, the absence of EG produces several large spheres with many thorns on the outside surface (Figure S1A, Electronic Supplementary Information, ESI), owing to the slow reduction kinetics without EG.[34] Besides, replacing EG with DMF induces the formation of serious aggregated nanoparticles (Figure S1B, ESI), revealing the critical role of EG in dispersing Pt-Pd nanoparticles.

Most importantly, the absence of *N*-methylimidazole yields lots of aggregated nanospheres (Figure S2A, ESI), without any branched shape formed. Increasing the concentration of *N*-methylimidazole to 1.32 M produces some shorter branches (Figure S2B, ESI) as compared to the best ones under the standard conditions with 3.14 M *N*-methylimidazole (Figure 1B). This is ascribed to the relaxed growth with insufficient *N*-methylimidazole.[29] Alternatively, excess *N*-methylimidazole such as 4.37 M causes hierarchy overgrowth along the (111) planes, leading to the formation of Pt-Pd nanocrystals with much longer arms (Figure S2C, ESI). These observations strongly demonstrate the essential role of *N*-methylimidazole as a structure-directing agent for selective adsorption on the specific metallic crystal planes.[35, 36]

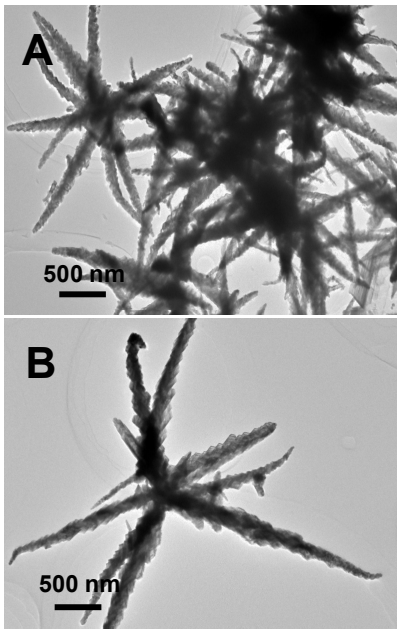

Figure 3. TEM images of the products collected by using H_2PtBr_6 and Na_2PdBr_4 (A), K_2PtI_6 and PdI_2 (B) as precursors.

To elucidate the precursor-dependent shape control, we chose different precursors, while kept all the other synthetic conditions unchanged. Interestingly, the arms of Pt-Pd multipods increase in the order of using chlorate salts (Figure 1B), bromate salts (Figure 3A), and iodate salts (Figure 3B), while the highly branched morphology almost unvaried, owing to the different adsorption effects.[37] It indicates that the halide precursors control the growth rates of the branches.

Alternatively, only using $PdCl_2$ as the precursor causes the formation of agminated nanoparticles with short branches (Figure S3, ESI), while nearly no product is obtained for H_2PtCl_6 as the precursor. This is ascribed to the relatively lower standard reduction potential of $PtCl_6^{2-}$/Pt (0.73 V *vs*. SHE) than that of Pd^{2+}/Pd (0.92 V *vs*. SHE). These observations verify the key role of Pd in the nucleation process,[35] while Pt promotes the growth rate through binding with *N*-methylimidazole.[38] On the other hand, using $Pt(acac)_2$ and $Pd(acac)_2$ as the precursors, rather than H_2PtCl_6 and $PdCl_2$, only some irregular structures are formed, instead of Pt-Pd multipods (Figure S4, ESI). It is attributed to the variation of reduction kinetics by using different precursors.[39]

Time-dependent TEM experiments were performed to monitor the morphology evolution of Pt-Pd multipods during the hydrothermal process. As illustrated in Figure 4, numerous scattered nanoparticles are emerged after the reaction of 1 h

(Figure 4A), which are gradually aggregated together to form polyhedron nuclei within the reaction time of 2 h (Figure 4B) via heterogeneous nucleation and self-assembly.[40] The newly generated Pt and Pd atoms grow along the (111) planes from the initial nuclei, with the orientation role of Pt precursor-*N*-methylimidazole complex that can decrease the surface energy of the present system.[24, 38, 41] Immature multipods of Pt-Pd nanocrystals are generated by increasing the reaction time to 4 h (Figure 4C), and their arms continually increase with the reaction time even up to 6 h (Figure 1B), owing to the subsequent attachment of newly formed Pt and Pd atoms onto the (111) planes.[42] Nevertheless, the shape of Pt-Pd nanocrystals almost remains unchanged by further prolonging the reaction time to 8 h (Figure 4D).

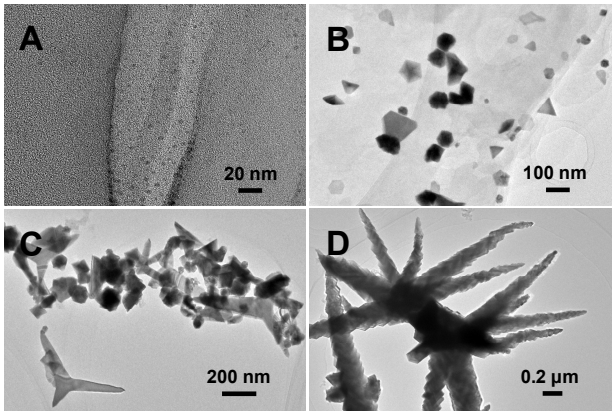

Figure 4. TEM images of the products collected at different reaction time: (A) 1 h, (B) 2 h, (C) 4 h, and (D) 8 h.

Figure 5 describes the formation mechanism of Pt-Pd multipods. The Pt and Pd precursors are gradually reduced to Pt and Pd atoms by EG. Meanwhile, the Pt precursor-*N*-methylimidazole complex is formed to direct the subsequent crystal growth, owing to its stronger binding affinity to N-containing molecules in comparison with that of the Pd precursor.[38, 43] Once the concentrations of the newly formed Pt and Pd atoms achieve the level of supersaturation, they begin to develop into polyhedral nuclei for decreasing the whole system surface free energy.[40] Afterward, the polyhedral nuclei undergo the epitaxial growth, along with elongating the corner of polyhedron.[27, 44] Last but not the least, Pt-Pd multipods with arms containing a succession of rhombohedral scleromeres are formed through multi-generation overgrowth at the tips and edges of the crystals.[45]

Figure S5 (ESI) shows the cyclic voltammograms (CVs) of Pt-Pd multipods (Figure S5A, ESI), Pt black (Figure S5B, ESI) and Pd black (Figure S5C, ESI) catalyst-modified electrodes in 0.5 M H_2SO_4 after the CO-stripping treatment. Based on the oxidation peak from the first (1st) cycle, the electrochemically active surface area (ECSA) of Pt-Pd multipods is calculated to be 20.6 $m^2\ g^{-1}$ (Figure S5D, ESI), which is much higher than those of Pt black (7.3 $m^2\ g^{-1}$) and Pd black (10.9 $m^2\ g^{-1}$).[35, 46, 47] It suggests more active sites available for Pt-Pd multipods in comparison with commercial Pt black and Pd black, which would endow them with improved electrocatalytic performance.[48]

Besides, the typical CVs of Pt-Pd multipods (curve a), Pt black (curve b) and Pd black (curve c) catalyst-modified electrodes were obtained in 0.5 M H_2SO_4 at a scan rate of 50 mV s^{-1} (Figure S6, ESI). All the samples display a strong peak, corresponding to proton reduction/hydrogen oxidation below 0.1 V.[49] The peak current densities in the hydrogen adsorption/desorption and oxide formation/reduction regions decrease in the order of Pt-Pd multipods, Pt black, and Pd black, strongly showing the larger ECSA of Pt-Pd multipods. It reveals that Pt-Pd multipods would have potential higher catalytic activity as a catalyst.[13]

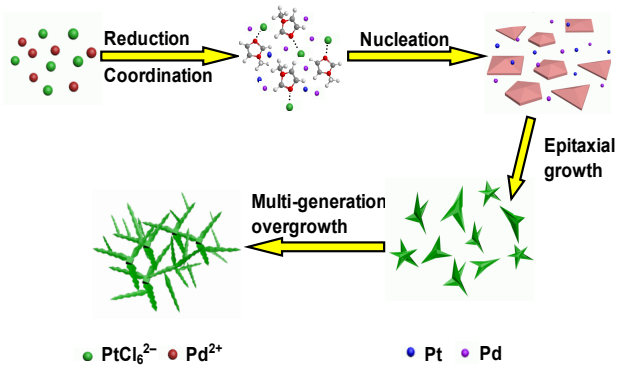

Figure 5. Schematic illustration for the formation mechanism of Pt-Pd multipods.

Herein, Pt-Pd multipods were applied as a catalyst for EG oxidation in alkaline media, using commercial Pt black and Pd black as references. As displayed in Figure 6A, each of them shows two obvious anodic peaks in their corresponding CVs, which are the typical features for EG oxidation during the forward and backward scans.[50] Clearly, Pt-Pd multipods exhibit the highest electrocatalytic current density among the catalysts, evidencing the enhanced catalytic activity of Pt-Pd multipods.[51]

Meanwhile, the onset potential of Pt-Pd multipods is ca. –0.71 V, which is more positive than Pt black (–0.75 V), but more negative than Pd black (–0.56 V). These phenomena strongly manifest the formation of Pt-Pd alloy, as supported by HAABF-STEM-EDS mapping images and XRD analysis. Furthermore, the ratio of the peak current densities associated with the anodic peaks in forward (j_F) and reverse (j_R) is 3.64 for Pt-Pd multipods, which is larger than Pd black (2.58), while smaller than Pt black (4.92) under the same conditions, owing to the modified electronic structure of Pt by the introduction of Pd. Additionally, the value of j_F/j_R of Pt-Pd multipods is much higher than those of SF-MWCNT-Pd (1.82),[52] Pd/C (2.74),[53] S-MWNTs/Pd (1.94),[54] and hAg@Pt–RGO (1.72) in the literature,[55] illustrating better CO resistance activity of Pt-Pd multipods.[56]

To compare the catalytic activity for different catalysts, the current densities of anodic peak for Pt-Pd multipods, Pt black, and Pd black were normalized with respect to the loading amount and ECSA of a catalyst, respectively. As listed in Figure 6B, the mass activity (current per unit gram of catalyst) of Pt-Pd multipods is higher than those of Pt black and Pd black. The specific activity (current per unit per surface area of catalyst) is slightly lower than that of Pt black, while higher than that of Pd

black. These results further demonstrate that Pt-Pd multipods have superior catalytic activity toward EG electrooxidation.

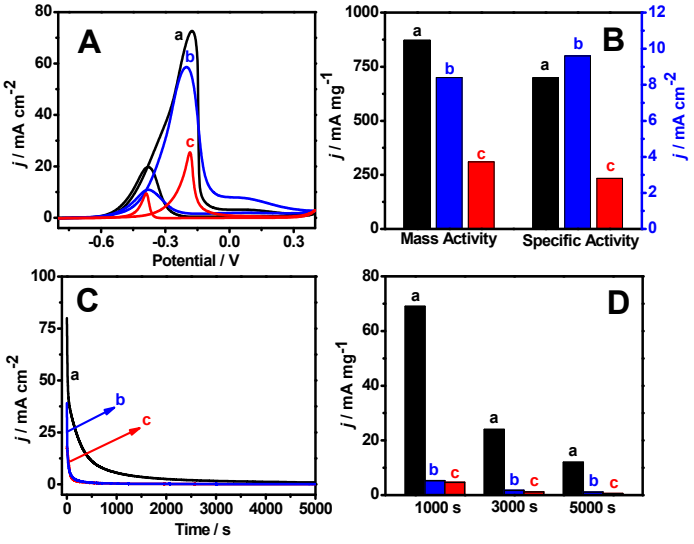

Figure 6. CVs (A) of the Pt-Pd multipods (curve a), Pt black (curve b), and Pd black (curve c) catalyst-modified electrodes in 1.0 M KOH + 1 M EG at a scan rate of 50 mV s^{-1}. The corresponding mass and specific activities (B) at the associated anodic peak potentials. The chronoamperometric curves (C) of the Pt-Pd multipods (curve a), Pt black (curve b), and Pd black (curve c) catalyst-modified electrodes at a fixed potential of –0.2 V. The corresponding mass activities (D) at different measured time.

The catalytic stability of Pt-Pd multipods, Pt black, and Pd black were examined by chronoamperometric experiments tested at –0.2 V for 5000 s (Figure 6C). Clearly, Pt-Pd multipods own higher catalytic current intensities and a slower dropping rate, compared with those of Pt black and Pd black under the identical conditions. Meanwhile, the corresponding mass activity of Pt-Pd multipods, Pt black, and Pd black were provided at the measured time of 1000, 3000, and 5000 s (Figure 6D). Obviously, Pt-Pd multipods decay much slower and remain comparatively higher mass activity after the chronoamperometric measurements, in comparison with those of Pt black and Pd black, revealing improved durability of Pt-Pd multipods.[57, 58]

To get deep insight into the catalytic durability of Pt-Pd multipods, the CVs were recorded in 1.0 M KOH containing 1 M EG for 2000 cycles, using Pt black and Pd black as referenced materials. It is found that the anodic peak current densities of Pt-Pd multipods remain 54.79 % and 44.04 % of the initial values after 1000 and 2000 cycles (Figure 7A), respectively. Nevertheless, the anodic peak current densities of Pt black (Figure 7B) and Pd black (Figure 7C) retain 0.052 % and 57.59 % after 1000 cycles, and 0.0096 % and 29.34 % after 2000 cycles, respectively. Additionally, the anodic peak current densities of Pt-Pd multipods slightly decrease over 2000 cycles (Figure 7D) as compared to Pt black and Pd black. These phenomena demonstrate the long-term durability of Pt-Pd multipods.[59]

All the above electrochemical experimental data confirm that Pt-Pd multipods can serve as an ideal catalyst for direct EG fuel cells, which would contribute to the following reasons. Firstly, Pt-Pd multipods possess much more accessible surface active sites because of their three-dimensional highly branched structures with various rhombohedral scleromeres.[60] Besides, the unique interconnected three-dimensional nanostructures make Pt-Pd multipods less vulnerable to dissolution and aggregation than those of the zero-dimensional Pt black and Pd black (Figure S7, ESI), and thereby improve its electrocatalytic stability.[9, 48] Moreover, the synergistic effects between Pt and Pd effectively enhance the electrocatalytic activity of Pt-Pd multipods.[11, 38]

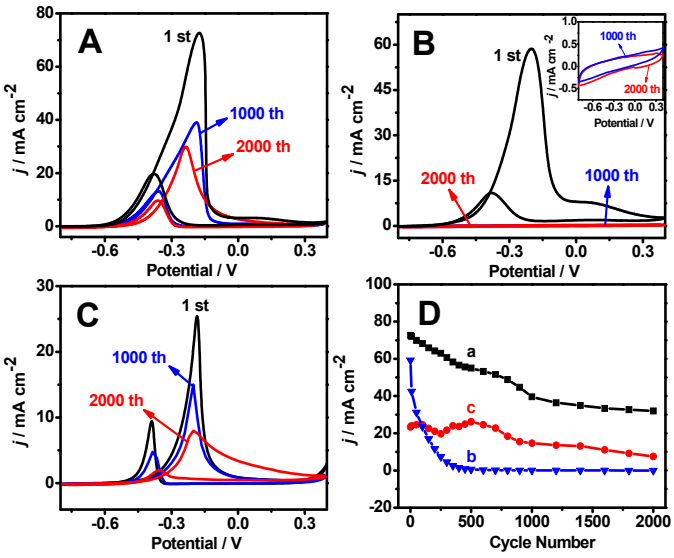

Figure 7. The 1st, 1000th, and 2000th CVs of the Pt-Pd multipods (A), Pt black (B) and Pd black (C) catalyst-modified electrodes in 1.0 M KOH + 1 M EG, respectively. The forward peak current density (*j*) as a function of potential scanning cycles (D) of the Pt-Pd multipods (curve a), Pt black (curve b), and Pd black (curve c) catalyst-modified electrodes. Inset in (B) show the corresponding high-resolution 1000th and 2000th CVs for Pt black catalyst-modified electrode.

Conclusions

In summary, we have developed a facile, efficient, and clean strategy for synthesis of three-dimensional Pt-Pd alloyed multipods under solvolthermal conditions by applying EG as a reducing agent and solvent, and *N*-methylimidazole as a structure-directing agent. The possible formation mechanism of Pt-Pd multipods was discussed, in which involves the nucleation, epitaxial growth, and multi-generation overgrowth processes. More importantly, the as-prepared Pt-Pd multipods displayed the enlarged ECSA, enhanced electrocatalytic activity, and long-term stability toward EG oxidation reaction, proving it as a highly efficient catalyst for direct alcohol fuel cells.

Acknowledgements

This work was financially supported by National Natural Science Foundation of China (21475118, 21175118 and 21275130) and colleges in Zhejiang province to the young academic leaders of academic climbing project (pd2013055).

Notes and references

College of Geography and Environmental Science, College of Chemistry and Life Science, Zhejiang Normal University, Jinhua 321004, China
**Corresponding Author: Tel./Fax:+86 579 82282269. Email: ajwang@zjnu.cn (AJW); jjfeng@zjnu.cn (JJF).*

1 L. Dai, Y. Zhao, Q. Chi, T. Huang and H. Liu, *CrystEngComm*, 2014, **16**, 5206-5211.
2 H. Zhang, M. Jin and Y. Xia, *Chem. Soc. Rev.*, 2012, **41**, 8035-8049.
3 X. Liu, D. Wang and Y. Li, *Nano Today*, 2012, **7**, 448-466.
4 Y. Liu, D. Li and S. Sun, *J. Mater. Chem.*, 2011, **21**, 12579-12587.
5 N. S. Porter, H. Wu, Z. Quan and J. Fang, *Acc. Chem. Res.*, 2013, **46**, 1867-1877.
6 Y.-W. Lee, A. R. Ko, D.-Y. Kim, S.-B. Han and K.-W. Park, *RSC Adv.*, 2012, **2**, 1119-1125.
7 Y. Yamauchi, A. Tonegawa, M. Komatsu, H. Wang, L. Wang, Y. Nemoto, N. Suzuki and K. Kuroda, *J. Am. Chem. Soc.*, 2012, **134**, 5100-5109.
8 Y.-Y. Feng, L.-X. Bi, Z.-H. Liu, D.-S. Kong and Z.-Y. Yu, *J. Catal.*, 2012, **290**, 18-25.
9 X. Huang, E. Zhu, Y. Chen, Y. Li, C.-Y. Chiu, Y. Xu, Z. Lin, X. Duan and Y. Huang, *Adv. Mater.*, 2013, **25**, 2974-2979.
10 A.-X. Yin, X.-Q. Min, W. Zhu, H.-S. Wu, Y.-W. Zhang and C.-H. Yan, *Chem. Commun.*, 2012, **48**, 543-545.
11 Z.-C. Zhang, J.-F. Hui, Z.-G. Guo, Q.-Y. Yu, B. Xu, X. Zhang, Z.-C. Liu, C.-M. Xu, J.-S. Gao and X. Wang, *Nanoscale*, 2012, **4**, 2633-2639.
12 Z. Chen, M. Waje, W. Li and Y. Yan, *Angew. Chem. Int. Ed.*, 2007, **46**, 4060-4063.
13 L. Wang and Y. Yamauchi, *Chem. Mater.*, 2009, **21**, 3562-3569.
14 B. Lim and Y. Xia, *Angew. Chem. Int. Ed.*, 2011, **50**, 76-85.
15 B. Lim, M. Jiang, P. H. C. Camargo, E. C. Cho, J. Tao, X. Lu, Y. Zhu and Y. Xia, *Science*, 2009, **324**, 1302-1305.
16 X. Chen, Z. Cai, X. Chen and M. Oyama, *J. Mater. Chem. A*, 2014, **2**, 315-320.
17 B. Liu, H. Y. Li, L. Die, X. H. Zhang, Z. Fan and J. H. Chen, *J. Power Sources*, 2009, **186**, 62-66.
18 H. Zhang, M. Jin, H. Liu, J. Wang, M. J. Kim, D. Yang, Z. Xie, J. Liu and Y. Xia, *ACS Nano*, 2011, **5**, 8212-8222.
19 S. Guo, S. Dong and E. Wang, *Chem. Commun.*, 2010, **46**, 1869-1871.
20 X. Chen, Z. Cai, X. Chen and M. Oyama, *Carbon*, 2014, **66**, 387-394.
21 S. Guo, S. Dong and E. Wang, *ACS Nano*, 2009, **4**, 547-555.
22 S.-S. Li, J.-N. Zheng, X. Ma, Y.-Y. Hu, A.-J. Wang, J. Chen and J.-J. Feng, *Nanoscale*, 2014, **6**, 5708-5713.
23 T. Kim, J. Lian, J. Ma, X. Duan and W. Zheng, *Cryst. Growth Des.*, 2010, **10**, 2928-2933.
24 R. Zhao, G. Fu, T. Zhou, Y. Chen, X. Zhu, Y. Tang and T. Lu, *Nanoscale*, 2014, **6**, 2776-2781.
25 G. Fu, X. Jiang, M. Gong, Y. Chen, Y. Tang, J. Lin and T. Lu, *Nanoscale*, 2014, **6**, 8226-8234.
26 X. Yang, Q. Yang, J. Xu and C.-S. Lee, *J. Mater. Chem.*, 2012, **22**, 8057-8062.
27 S. Maksimuk, X. Teng and H. Yang, *J. Phys. Chem. C*, 2007, **111**, 14312-14319.
28 Y. Lu, Y. Jiang and W. Chen, *Nano Energy*, 2013, **2**, 836-844.
29 H. Zhu, G. Li, X. Lv, Y. Zhao, T. Huang, H. Liu and J. Li, *RSC Adv.*, 2014, **4**, 6535-6539.
30 B. Y. Xia, H. B. Wu, Y. Yan, X. W. Lou and X. Wang, *J. Am. Chem. Soc.*, 2013, **135**, 9480-9485.
31 J. Yang, W. Zhou, C. H. Cheng, J. Y. Lee and Z. Liu, *ACS Appl. Mat. Interfaces*, 2010, **2**, 119-126.
32 G. Fu, K. Wu, J. Lin, Y. Tang, Y. Chen, Y. Zhou and T. Lu, *J. Phys. Chem. C*, 2013, **117**, 9826-9834.
33 Y. Lu, Y. Jiang and W. Chen, *Nanoscale*, 2014, **6**, 3309-3315.
34 L. S. Sarma, C.-H. Chen, S. M. S. Kumar, G.-R. Wang, S.-C. Yen, D.-G. Liu, H.-S. Sheu, K.-L. Yu, M.-T. Tang, J.-F. Lee, C. Bock, K.-H. Chen and B.-J. Hwang, *Langmuir*, 2007, **23**, 5802-5809.
35 J.-J. Lv, J.-N. Zheng, S.-S. Li, L.-L. Chen, A.-J. Wang and J.-J. Feng, *J. Mater. Chem. A*, 2014, **2**, 4384-4390.
36 J.-J. Lv, J.-N. Zheng, Y.-Y. Wang, A.-J. Wang, L.-L. Chen and J.-J. Feng, *J. Power Sources*, 2014, **265**, 231-238.
37 M. Chen, B. Wu, J. Yang and N. Zheng, *Adv. Mater.*, 2012, **24**, 862-879.
38 S. W. Kang, Y. W. Lee, Y. Park, B.-S. Choi, J. W. Hong, K.-H. Park and S. W. Han, *ACS Nano*, 2013, **7**, 7945-7955.
39 X. Huang, H. Zhang, C. Guo, Z. Zhou and N. Zheng, *Angew. Chem. Int. Ed.*, 2009, **48**, 4808-4812.
40 Y. Wang, S.-I. Choi, X. Zhao, S. Xie, H.-C. Peng, M. Chi, C. Z. Huang and Y. Xia, *Adv. Funct. Mater.*, 2014, **24**, 131-139.
41 B. Lim, M. Jiang, T. Yu, P. C. Camargo and Y. Xia, *Nano Res.*, 2010, **3**, 69-80.
42 S. Maksimuk, X. Teng and H. Yang, *Phys. Chem. Chem. Phys.*, 2006, **8**, 4660-4663.
43 C. J. DeSantis, A. A. Peverly, D. G. Peters and S. E. Skrabalak, *Nano Lett.*, 2011, **11**, 2164-2168.
44 L. Zhang, S.-I. Choi, J. Tao, H.-C. Peng, S. Xie, Y. Zhu, Z. Xie and Y. Xia, *Adv. Funct. Mater.*, 2014, **24**, 7520-7529.
45 W. Wang, Y. Han, M. Gao and Y. Wang, *CrystEngComm*, 2013, **15**, 2648-2656.
46 M. J. Watt-Smith, J. M. Friedrich, S. P. Rigby, T. R. Ralph and F. C. Walsh, *J. Phys. D: Appl. Phys.*, 2008, **41**, 174004-174012.
47 C. Hu, Z. Bai, L. Yang, J. Lv, K. Wang, Y. Guo, Y. Cao and J. zhou, *Electrochim. Acta*, 2010, **55**, 6036-6041.
48 X. Huang, Y. Li, Y. Chen, E. Zhou, Y. Xu, H. Zhou, X. Duan and Y. Huang, *Angew. Chem.*, 2013, **125**, 2580-2584.
49 C. Zhu, S. Guo and S. Dong, *Chem. Eur. J.*, 2013, **19**, 1104-1111.
50 V. Selvaraj, M. Vinoba and M. Alagar, *J. Colloid Interface Sci.*, 2008, **322**, 537-544.
51 F. Li, Y. Guo, R. Li, F. Wu, Y. Liu, X. Sun, C. Li, W. Wang and J. Gao, *J. Mater. Chem. A*, 2013, **1**, 6579-6587.
52 T. Ramulifho, K. I. Ozoemena, R. M. Modibedi, C. J. Jafta and M. K. Mathe, *J. Electroanal. Chem.*, 2013, **692**, 26-30.
53 O. O. Fashedemi and K. I. Ozoemena, *Electrochim. Acta*, 2014, **128**, 279-286.
54 Z.-P. Sun, X.-G. Zhang, Y.-Y. Liang and H.-L. Li, *J. Power Sources*, 2009, **191**, 366-370.
55 J.-N. Zheng, J.-J. Lv, S.-S. Li, M.-W. Xue, A.-J. Wang and J.-J. Feng, *J. Mater. Chem. A*, 2014, **2**, 3445-3451.
56 Y.-N. Wu, S.-J. Liao, Z.-X. Liang, L.-J. Yang and R.-F. Wang, *J.*

Power Sources, 2009, **194**, 805-810.
57 B. Y. Xia, H. B. Wu, X. Wang and X. W. Lou, *J. Am. Chem. Soc.*, 2012, **134**, 13934-13937.
58 F. Zhan, T. Bian, W. Zhao, H. Zhang, M. Jin and D. Yang, *CrystEngComm*, 2014, **16**, 2411-2416.
59 C. Hu, H. Cheng, Y. Zhao, Y. Hu, Y. Liu, L. Dai and L. Qu, *Adv. Mater.*, 2012, **24**, 5493-5498.
60 K. Kakaei, *Carbon*, 2013, **51**, 195-201.